University of Nebraska - Lincoln

DigitalCommons@University of Nebraska - Lincoln

2019

Atomic-scale control of magnetism at the titanite-manganite interfaces

H. Wang, X. Chi, Z. R. Liu, H. Y. Yoong, L. L. Tao, J. X. Xiao, R. Guo, J. X. Wang, Z. L. Dong, P. Yang, C. J. Sun, J. Wang, G. M. Chow, E. Y. Tsymbal, H. Tian, and J. S. Chen

Atomic-Scale Control of Magnetism at the Titanite-Manganite Interfaces

Han Wang,[†,○] Xiao Chi,[‡,§,○] ZhongRan Liu,[#,○] HerngYau Yoong,[†] LingLing Tao,[∥] JuanXiu Xiao,[†] Rui Guo,[†] JingXian Wang,[¶] ZhiLi Dong,[¶] Ping Yang,[§] Cheng-Jun Sun,[∇] ChangJian Li,[†] XiaoBing Yan,[⊥] John Wang,[†] Gan Moog Chow,[†] Evgeny Y. Tsymbal,[∥] He Tian,*[,#] and Jingsheng Chen*[,†]

[†]Department of Materials Science and Engineering, National University of Singapore, 117575 Singapore

[‡]Department of Physics, National University of Singapore, 2 Science Drive 3, 117542 Singapore

[#]Center of Electron Microscope, State Key Laboratory of Silicon Materials, School of Materials Science and Engineering, Zhejiang University, Hangzhou 310027, China

[∥]Department of Physics and Astronomy and Nebraska Center for Materials and Nanoscience, University of Nebraska, Lincoln, Nebraska 68588-0299, United States

[¶]School of Materials Science and Engineering, Nanyang Technological University, 639798 Singapore

[§]Singapore Synchrotron Light Source (SSLS), National University of Singapore, 117603 Singapore

[∇]Advanced Photon Source, Argonne National Laboratory, Argonne, Illinois 60439, United States

[⊥]College of Electron and Information Engineering, Hebei University, Baoding 071002, China

S *Supporting Information*

ABSTRACT: Complex oxide thin-film heterostructures often exhibit magnetic properties different from those known for bulk constituents. This is due to the altered local structural and electronic environment at the interfaces, which affects the exchange coupling and magnetic ordering. The emergent magnetism at oxide interfaces can be controlled by ferroelectric polarization and has a strong effect on spin-dependent transport properties of oxide heterostructures, including magnetic and ferroelectric tunnel junctions. Here, using prototype $La_{2/3}Sr_{1/3}MnO_3/BaTiO_3$ heterostructures, we demonstrate that ferroelectric polarization of $BaTiO_3$ controls the orbital hybridization and magnetism at heterointerfaces. We observe changes in the enhanced orbital occupancy and significant charge redistribution across the heterointerfaces, affecting the spin and orbital magnetic moments of the interfacial Mn and Ti atoms. Importantly, we find that the exchange coupling between Mn and Ti atoms across the interface is tuned by ferroelectric polarization from ferromagnetic to antiferromagnetic. Our findings provide a viable route to electrically control complex magnetic configurations at artificial multiferroic interfaces, taking a step toward low-power spintronics.

KEYWORDS: *Ferroelectric field effect, orbital anisotropy, charge transfer, orbital hybridization, interfacial magnetic coupling, artificial multiferroic interface*
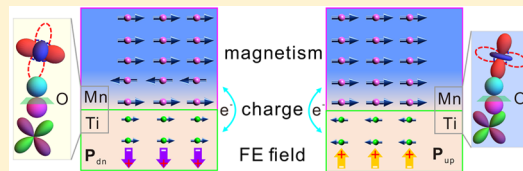
Multiferroics, compounds with two or more ferroic orders, have potential applications in electric-field-controlled spintronic devices with ultralow energy consumption.[1−3] Owing to the scarcity of single-phase materials with strong magnetoelectric coupling, the investigation of artificial multiferroic heterostructures, consisting of ferromagnetic (FM) and ferroelectric (FE) layers, has received much attention.[4−9] Extensive studies have focused on the influence of FE polarization on magnetism via strain coupling,[10−12] interfacial-oxidized state,[9] exchange coupling,[13] interfacial orbital reconstructions,[14] interfacial bond reconfiguration,[8] carrier density modulation (charge transfer),[6,12,15] or a combination of these at heterointerfaces. For example, (i) Cui et al. have demonstrated a FE-polarization control of interfacial orbital reconstruction and its effect on transport of

contacted films;[14] (ii) Molegraaf et al. have proposed charge-density-driven magnetic ground states;[15] (iii) Bingham et al. have attributed the enhanced magnetocaloric effect to the strain effect from FE capping layer;[12] and (iv) Herklotz et al. have presented a reversible control of interfacial magnetism through ionic-liquid-assisted polarization switching.[16] Still, however, there is a limited understanding of the FE field effect on orbital hybridizations affecting the interfacial magnetism and the exchange coupling, despite the observation of interfacial magnetism in FM/FE systems.[12,17] Moreover, the
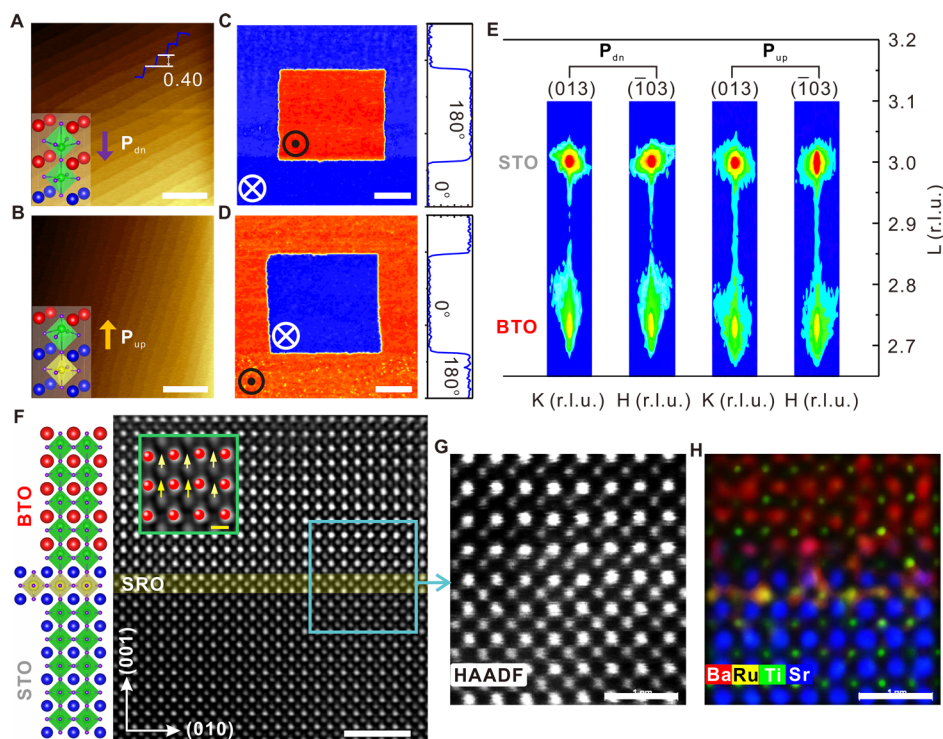
Figure 1. Ferroelectricity and structural characterization of LSMO/BTO heterostructures. (A) and (B) The surface morphology of heterostructures on TiO_2- and SrO-terminated STO substrates, respectively. The insets show the schematic illustrations of preferential FE polarization. The scale bar is 0.5 μm. (C) and (D) Typical out-of-plane PFM phase images of 45 u.c. BTO with downward polarization (P_{dn}) and upward polarization (P_{up}), respectively. The square domains are written using a conductive AFM tip with $\mp$6 V bias. The scale bar is 1 μm. (E) In plane asymmetric RSMs around the (013) and ($\bar{1}$03) Bragg reflections of the heterostructures. (F) Typical atomic-resolution HAADF-STEM image of the heterostructure terminated by SrO along the [001] zone axis, together with a schematic illustration of the termination transformation from TiO_2 to SrO by predepositing 1 u.c. $SrRuO_3$ (SRO) on STO. The scale bar is 2 nm. The inset in the green rectangle shows the superposition of the magnified STEM image of the overlying area and Ti displacement vector maps (yellow arrow). The yellow scale bar is 40 pm. (G) and (H) A magnified image and false-color overlaid EDX elemental maps from an area marked with a cyan rectangle in (F), respectively. The scale bar is 1 nm.

control of magnetic coupling and electronic structure at multiferroic interfaces deserves particular attention, since they may directly influence spin-dependent transport properties[18] and the performance of practical oxide devices.[6] The insight into the competition between charge transfer due to valence imbalance and carrier-density modulation caused by the FE field as well as the control of the interfacial magnetic coupling, therefore, is warranted in realizing potential applications of multiferroic heterostructures.

Furthermore, the extensive studies of the magnetoelectric coupling in high-quality thick piezoelectric or FE layers (even substrates) have shown that high electrical voltage is essential for the magnetoelectric effect,[10,15] thus introducing other undesirable effects, such as strain effect via electrostriction,[10] oxygen vacancy migration,[19] and carrier modulation.[20] The multidomain state in a thick FE layer also complicates the effect of FE polarization on interfacial magnetism.[21] To obtain the FE field effect, a series of samples with opposite spontaneous FE polarization states but with the same strain state are needed. To avoid this complexity, we have fabricated the prototypical heterostructures of FM $La_{0.7}Sr_{0.3}MnO_3$ (LSMO) and FE $BaTiO_3$ (BTO), carrying different polarizations via interface engineering,[22,23] instead of using an applied electric field. To separate the possible effects of the interface chemistry, another series of heterostructures, exhibiting no FE polarization but having the same interface atomic-plane stacking sequence with that of BTO thicker films, were fabricated and explored.

In this work, we demonstrate the FE field-dependent orbital hybridization affecting magnetism and exchange coupling at LSMO/BTO heterointerfaces by means of X-ray magnetic circular dichroism (XMCD). The changes of induced spin and orbital magnetic moments at Ti and Mn atoms are associated with the charge redistribution across the heterointerfaces. Combining the atomic-resolution energy dispersive X-ray (EDX) elemental maps and electron energy loss spectroscopy (EELS) data with aberration-corrected scanning transmission electron microscopy (STEM) results, the charge redistribution and the valence states at the LSMO/BTO interfaces are systematically analyzed. The modulation of the interfacial exchange interaction from FM to antiferromagnetic coupling originates from the change of orbital occupancy, as shown by X-ray linear dichroism (XLD) and theoretical calculations. These discoveries open the way for the electrical modulation of interfacial properties, especially on spin-dependent phenomena, at the atomic level.

Results. *Control of Ferroelectric Polarization via Interface Engineering.* We have in situ grown high-quality LSMO/BTO heterostructures on (001) $SrTiO_3$ (STO) substrates by pulsed laser deposition. For BTO, a thickness of 45 unit cells (u.c.) is chosen to keep sufficiently good FE properties with a single domain and fully strained state. For LSMO, a thickness of 5 u.c. is selected to ensure the collection of the interfacial layer signal using the total electron yield (TEY) measurements.[24,25] Figure 1A,B shows the morphology of LSMO/BTO heterostructure terminated by TiO_2 and SrO. Clear atomic
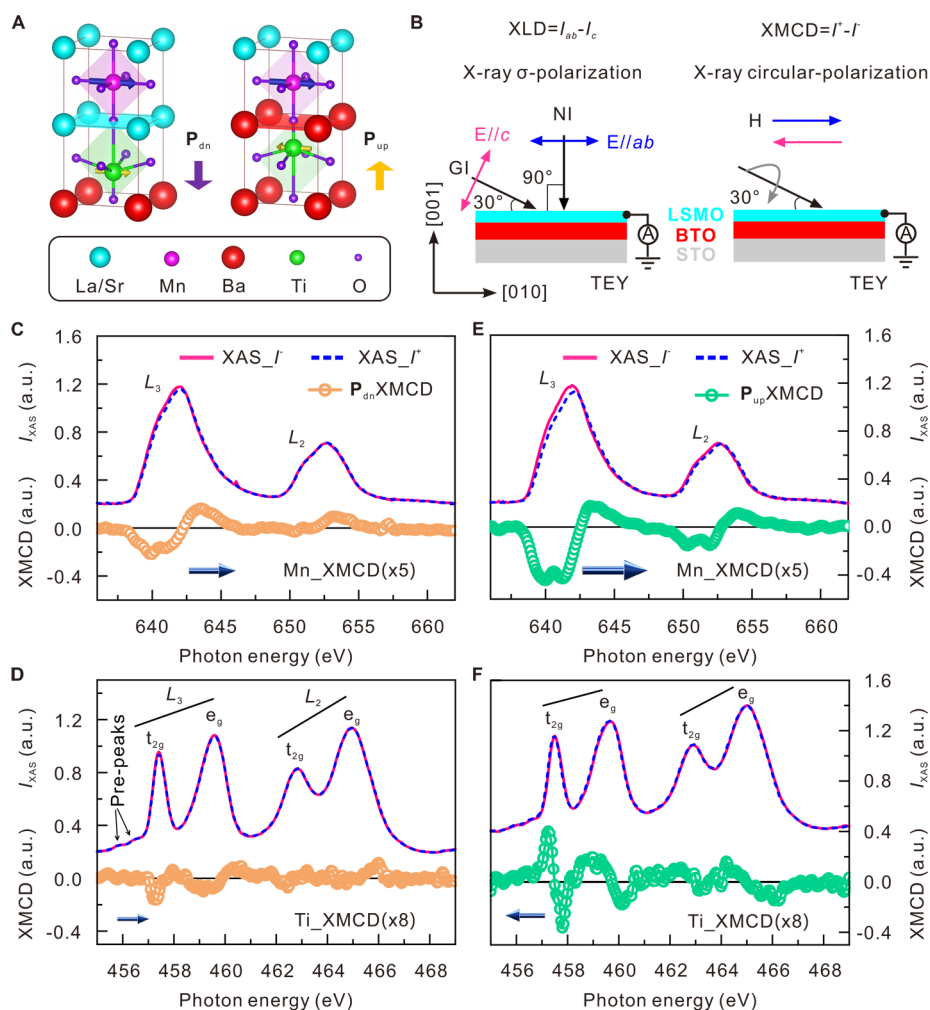
Figure 2. Normalized X-ray absorption spectroscopy and X-ray magnetic circular dichroism of the LSMO/BTO heterostructures at 80 K. (A) Schematic illustrations of the LSMO/BTO heterointerfaces and arrangement of magnetic moment dependent on FE polarization. (B) Principle of XLD and XMCD techniques, where GI and NI represent grazing incidence (polarization $E//c$) and normal incidence X-ray (polarization $E//ab$), respectively. (C) and (D) Mn- and Ti-$L_{2,3}$ edges XAS under ± 1 T in-plane magnetic field and their XMCD of LSMO/BTO with a downward polarization. (E) and (F) Mn- and Ti-$L_{2,3}$ edges XAS under ± 1 T in-plane magnetic field and their XMCD of LSMO/BTO with an upward polarization. The arrows in the inset show the direction of the total magnetic moment at Ti and Mn.

terrace separated by ∼0.40 ± 0.05 nm high step reveals a two-dimensional growth of films, which is further supported by in situ RHEED of various oxide materials (Figure S1). We obtained the SrO-terminated surface through depositing a 1 u.c.-SrRuO$_3$ (SRO) layer on TiO$_2$-terminated STO substrates at high temperature and low oxygen pressure (Figure S1), benefiting from that, a highly volatile RuO$_2$-layer will be desorbed before the deposition of BTO film.[23] The out-of-plane piezoresponse force microscopy (PFM) images of BTO written by an electrical bias of ∓6 V at room temperature are shown in Figure 1C,D. A clear phase contrast of ∼180° shows high quality and switchability of FE polarization in BTO films, which is further supported by the butterfly-like amplitude and hysteresis phase loop (Figure S2A,B). More importantly, we deduce that the FE polarization of BTO terminated by SrO, which is switched by a positive electrical bias through Coulomb interaction between the conductive tip and bound charges, is upward ($\mathbf{P}_{up}$), whereas the FE polarization of BTO terminated by TiO$_2$ which is switched by a negative electrical bias is downward ($\mathbf{P}_{dn}$), as shown in Figure S3. Thus, we could conclude that the preferential FE polarization in the as-grown

BTO terminated by TiO$_2$ (SrO) has a $\mathbf{P}_{dn}$ ($\mathbf{P}_{up}$) state.[22,26] We also confirm that the 5 u.c. LSMO does not influence the original orientation of the FE polarization in BTO, as shown in Figure S2B−E. Concerning the effect of temperature on the ferroelectricity of fully stained films, the remnant polarization (without electrical bias)[27] has an increasing trend with decreasing temperature, revealing no structural phase transition. On the other hand, theoretical calculations suggest that ultrathin BTO films keep the c-axis tetragonal structure, and FE polarization does not rotate at low temperature due to a compressive strain of −2.0% imposed by epitaxy with STO substrate.[28] Hence, it is reasonable that BTO films retain a single FE domain ($\mathbf{P}_z > \mathbf{P}_x = \mathbf{P}_y = 0$) from room temperature to 80 K. Reciprocal space mappings (RSMs) shown in Figure 1E and Figure S4 suggest that both BTO films are coherently grown on TiO$_2$- and SrO-terminated STO substrates. The as-grown films have a tetragonal structure under the compressive strain of −2.22% (Table S1) and possess the almost same strained state (lattice parameters: $a = b = 3.905$ Å, $c = 4.348$ Å, and tetragonality = 1.11), as indicated by the same $\mathbf{L}$ values. In comparison with the lattice parameters of BTO and STO, the
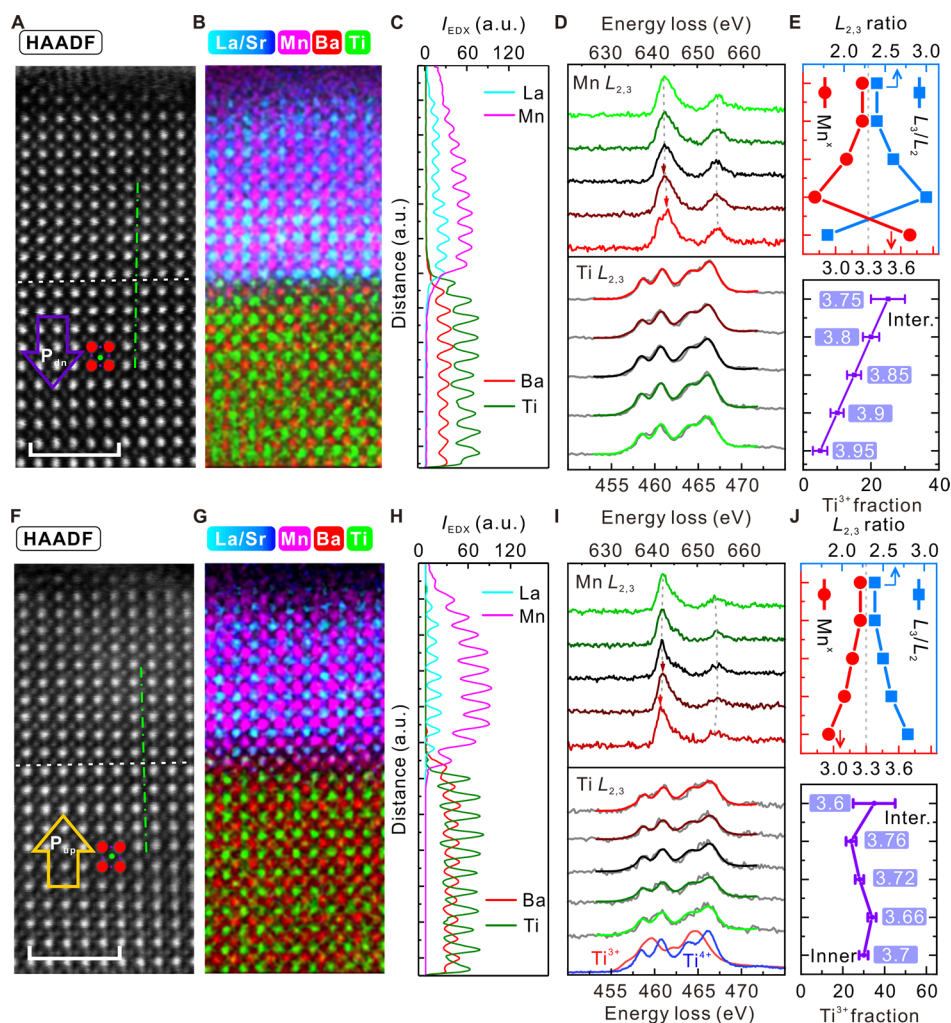
Figure 3. STEM, EDX, and EELS across the LSMO/BTO heterointerface. (A–E) under P_{dn} state. (A) The HAADF image. The white dashed line represents the position of the interface. The green dot-dashed line denotes the electron beam position for the EELS spectra. The scale bar is 2 nm. (B) The atomic-resolution overlaid EDX elemental maps. (C) EDX elemental profiles extracted from La-*L* (Cyan), Ba-*M* (Red), Mn-*K* (Pink), and Ti-*K* (Green) edges. (D) Layer-resolved EELS spectra of Mn-$L_{2,3}$ edges (top) and Ti-$L_{2,3}$ edges (bottom). The gray dashed lines mark the position of L_3 and L_2 peaks for Mn-$L_{2,3}$ edges. The gray lines for Ti-$L_{2,3}$ edges represent experimental data, while the colored lines are the fitted results by the fractional contribution of Ti^{4+} and Ti^{3+}. Reference spectra for Ti^{3+} (Red line) and Ti^{4+} (blue line) are shown at the bottom, taken from Ti_2O_3 powder and stoichiometric $SrTiO_3$ substrate, respectively. (E) The extracted $L_{2,3}$ ratio from EELS of Mn and the calculated Mn valence state vs the distance from the surface. The gray dashed line shows the Mn valence state (3.3) in bulk LSMO (top). The component of Ti from EELS of Ti-*L* edge vs the distance from the interface (bottom). The numbers in the inset represent the calculated Ti valence state. (F–J) Under the P_{up} state.

LSMO layers on top of them are under tensile strain (0.6%), as shown in Figure S4C. Considering almost the same strained BTO, we deduce that LSMO layers also have the same stress state except for the interfacial unit cell, being sensitive to the FE field.

Figure 1F and Figure S5 show typical cross-section scanning transmission electron microscopy (STEM) images of a LSMO/BTO heterostructure on a SrO-terminated STO substrate, directly revealing the quality of film and FE displacement of Ti ions (D_{Ti}). The FE polarization can be roughly evaluated using the empirical linear relation ($P_s = \kappa * D_{Ti}$), where P_s represents the spontaneous polarization, and κ is a constant of 2.0 $\mu C/cm^2$/pm used in the estimation of P_s for BTO, PTO, and BFO systems.[29] The FE polarization of BTO film is calculated to be about 50 $\mu C/cm^2$, close to the reported values of BTO film.[30] The clear contrast from the high-angle annular dark-field STEM (HAADF-STEM) images in Figure 1G shows the predeposited 1 u.c. SRO with Ru

vacancies, further confirmed by EDX map in Figure 1H. Note that, Sr is brighter than Ru, unlike the perfect SRO crystal (Figure S13), which is associated with reducing scattering due to Ru vacancies. The same batch of LSMO/BTO heterostructures with TiO_2 termination is grown at the same conditions with that of the SrO terminated heterostructure, revealing the same strain state through synchrotron XRD (Figure S4) and STEM images (Figure S6). We, therefore, are able to manipulate the FE polarization of BTO under the same strained state only by engineering the interface chemical environment, without an external electric field.

Effect of Polarization on the Orbital Hybridization and Induced Magnetism at Heterointerface. X-ray absorption spectroscopy (XAS) and XMCD techniques are used to probe the element-resolved magnetic moments in the heterostructures, taking advantage of the elemental specificity and shallow probing depth of XAS in the total electron yield (TEY) mode (details in Materials and Methods and Supporting Informa-

tion). Figure 2 displays normalized XAS and XMCD of Mn- and Ti-$L_{2,3}$ edges in LSMO/BTO heterostructures with $\mathbf{P}_{dn}$ and $\mathbf{P}_{up}$ states (Figure 2A). The Mn XMCD signals in both samples with $\mathbf{P}_{dn}$ (Figure 2C) and $\mathbf{P}_{up}$ (Figure 2E) polarizations are similar to the typical XMCD spectrum, revealing robust Mn magnetism. In the BTO layer, the visible Ti XMCD signals (Figure 2D,F) indicate the presence of Ti magnetism at the heterointerfaces. Comparing the XMCD spectra of the samples with $\mathbf{P}_{up}$ and $\mathbf{P}_{dn}$ polarizations, the former seems to show a stronger signal. To gain a better insight into the influence of FE polarization on magnetism, we qualitatively compare the integrals of the XMCD signals (Figure S7). The result shows that the XMCD integrals for Mn are smaller for the $\mathbf{P}_{dn}$ state than that under the $\mathbf{P}_{up}$ state. More importantly, the XMCD integrals for Ti in the heterostructures with different FE polarizations display the opposite sign, whereas those for Mn in both samples display the same sign, which reveals the change of the exchange coupling between Mn and Ti. Though effective magnetic moments, using the spin and orbital sum rules[31] (details in Supporting Information), are greatly underestimated due to the strong L_2 and L_3 edges overlap for Ti and Mn, we only focus on the relative magnitude and sign of the spin (s_z) and orbital (l_z) moments (Table S2). We find that magnetic moments of Mn and Ti have both spin and orbital contributions under the $\mathbf{P}_{up}$ state resulting from strong orbital hybridization, contrary to the common belief that 3d transition metals should have a suppressed orbital moment owing to the quenched orbital angular momentum.

The macroscopic magnetic properties of multiferroic heterostructures (see Figures S8−S10) confirm the smaller magnetization under the $\mathbf{P}_{dn}$ state than that under the $\mathbf{P}_{up}$ state. As for the effect of FE polarization on the magnetic moment of Mn, there are two contributions affecting it. One is the valence change ($Mn^{3+} \leftrightarrow Mn^{4+}$) caused by the FE field through electrostatic doping.[15] Electrostatic doping results in hole accumulation under the $\mathbf{P}_{dn}$ state (more Mn^{4+}) and hole depletion under the $\mathbf{P}_{up}$ state (more Mn^{3+}) due to the screening of FE polarization. The other one is the FE field effect on the exchange coupling which changes from FM ($\mathbf{P}_{up}$, large e_g population) to AFM ($\mathbf{P}_{dn}$, small e_g population) through the change of the e_g population.[25,32,33] Surprisingly, a visible exchange bias is observed under the $\mathbf{P}_{dn}$ state, which experimentally supports the existence of an AFM layer at the Manganite/FE interface. The Ti magnetic moment is determined by the amount of transferred charge because of the interfacial hybridization between the Ti and Mn atoms. The hybridization of Mn and Ti is weaker in the LSMO/BTO interface with the $\mathbf{P}_{dn}$ state than that of the interface with the $\mathbf{P}_{up}$ state suggested by the XAS of O-K edge (Figure S18). The charge transfer is further confirmed by EELS results in Figure 3. Comparing with other similar systems,[16,25] our system has a larger change in magnetism for 5 u.c. LSMO. A possible reason is a smaller magnetization and thickness in our system that could be fully affected by the FE field effect.

To evaluate the effect of the interface chemistry on the magnetism of heterostructures, we have examined another group of samples grown under the same conditions, in which the thickness of BTO was decreased from 45 u.c. (much larger than the critical thickness, good ferroelectricity) to 3 u.c. (lower than the critical thickness,[34] very weak ferroelectricity as shown in Figure S11), but retaining the same chemical interface as for the samples in Figure 2. We found that Ti-L edge EELS throughout the BTO film (Figure S14) shows the

decreasing concentration of Ti^{3+} from the LSMO/BTO interface to the inside of BTO, suggesting that Ti^{3+} mainly appears at the interface. The XMCD spectra in Figure S12 display similar signals for Mn and almost negligible signals for Ti. These results suggest that the effects of the chemical properties at the interface would be too small to play any meaningful role on induced interfacial magnetism. Comparing to bulk BTO, which exhibits structural phase transitions,[10] the ultrathin single crystal films in our work are coherently grown on STO substrate (strain −2.0%). These fully strained films maintain the tetragonal structure in the range of 80−300 K due to the strong clamping effect of substrate.[30,35] The effect of strain on the magnetism of LSMO films is weak, unlike that on bulk BTO.

Note that a charge modulation mechanism of interfacial FM magnetic Ti in LaAlO₃/SrTiO₃[36] results from the polar discontinuity, and the theoretical calculations of Fe/BTO bilayers involve the mechanism of FE-induced charge transfer.[8] In the structure of Fe/BTO used by Valencia et al., the magnetic Ti at the interface is resulting from a proximity effect, and the finite magnetic moment is located at Fe and O atoms.[7] However, in LSMO/BTO heterointerfaces, charge redistribution is determined by the competition of charge transfer due to valence imbalance and carrier density modulation due to the FE field. Hence, the present magnetic arrangement is different from that discussed by Valencia et al.[7] and Duan et al.[8] where the alignment of the magnetic moments of Ti and Mn atoms is independent from the FE polarization and always antiparallel. The interfacial magnetic coupling in this work is similar to the one modulated by strain in the LaMnO₃/STO superlattice.[37] The critical difference is that exchange coupling between Ti and Mn at the artificial multiferroic interface is controlled by a FE field effect or electric field.

Ti and Mn Charge Redistribution Across the Interfaces. To probe the charge redistribution/oxidization state near the LSMO/BTO heterointerfaces, we conducted atomic-resolution EDX mapping and EELS characterization atomic layer by atomic layer, as shown in Figure 3. The HAADF image and EDX mapping of LSMO/BTO heterostructure under the $\mathbf{P}_{up}$ state in Figure 3A,B confirm that the LSMO layer was coherently grown on the BTO layer, retaining the tensile state. From the bottom to the top across the interface, the EELS signals gradually change from Ti-L edge to Mn-L edge, as shown in Figure 3D (top). To quantitatively obtain the fraction of Mn^{3+} and Mn^{4+}, the $L_{2,3}$ peak area ratio (L_3/L_2) is evaluated from the EELS of Mn through the Gaussian fitting of each individual Mn peak L_2 and L_3, as shown in Figure S15, following the work of Varela et al.[38] It can be seen that the $L_{2,3}$ ratio decreases within 2 u.c. near the LSMO/BTO interface, indicating the increase of the Mn valence as shown in Figure 3E (top). This agrees with the peak position shift seen in Figure 3D (top). For the BTO layer, the Ti-$L_{2,3}$ edge spectra shown in Figure 3D (bottom) were decomposed into a linear combination of the reference data for Ti^{3+} and Ti^{4+}, as shown in Figure S16, following the work of Ohtomo et al.[39] The fraction of Ti^{3+} gradually increases from the inside of the BTO to the LSMO/BTO interface, indicating the decrease of the Ti valence from +4 as shown in Figure 3E (bottom). Quantitatively analyzing the EELS spectra of Mn and Ti, we argue the existence of charge redistribution, originating from the competition of valence imbalance (-(BaO)⁰-(TiO₂)⁰-(La/ Sr O)$^{+0.67}$-(MnO₂)$^{-0.67}$-) and FE polarization discontinuity at the heterointerface. This valence imbalance may induce a
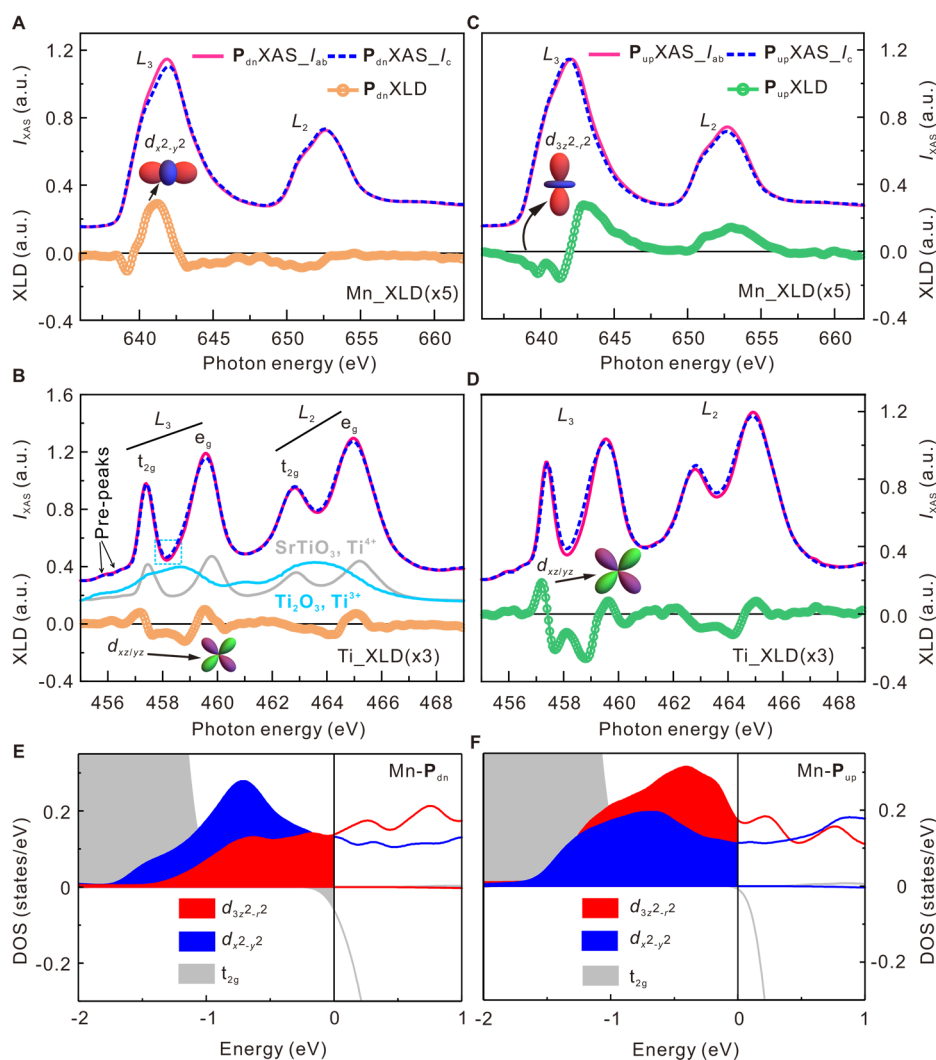
Figure 4. Normalized X-ray absorption spectroscopy and X-ray linear dichroism of the LSMO/BTO heterostructures at 300 K. (A) and (B) Mn- and Ti-$L_{2,3}$ edge XAS and their XLD for LSMO/BTO under the P_{dn} state, respectively. The blue line and gray line represent Ti-L edge XAS for the reference samples of $SrTiO_3$ and Ti_2O_3, respectively. (C) and (D) Mn- and Ti-$L_{2,3}$ edge XAS and their XLD for LSMO/BTO under the P_{up} state, respectively. The insets show the preferential orbitals of Ti and Mn under different polarization states, respectively. (E) and (F) The orbital-resolved DOS in the LSMO/BTO heterostructure projected onto the interfacial Mn atoms at the LaO/TiO interface (E) and the BaO/MnO interface (F).

charge transfer/oxygen vacancy,[40] whereas the FE polarization discontinuity may induce screening charges[41] at the interface. Comparing to the LSMO/BTO heterointerface under P_{dn} state, $L_{2,3}$ ratio extracted from the EELS of Mn, shown in Figure 3I (top), gradually decreases from the LSMO/BTO interface to the surface, indicating the gradual increase of Mn valence as shown in Figure 3J (top). Also, there is a more significant fraction of Ti^{3+} at the heterointerface, therefore, indicating a lower Ti valence. On one hand, both heterointerfaces under the P_{dn} and P_{up} states have Mn and Ti valence changes, in turn, leading to induced magnetism at the heterointerfaces. On the other hand, our EELS analysis indicates the affected thickness of Mn valence and change of Ti valence at the LSMO/BTO heterointerface under the P_{up} state are more significant than that at the heterointerface under the P_{dn} state due to a larger charge redistribution arising from the stronger Mn−O−Ti hybridization. This enhancement is caused by the FE field, resulting in a more considerable interfacial magnetism.

Mn−O Bonds and Orbital Occupancy Tuned by Ferroelectric Field Effect. The physical properties (such as magnetic interaction and electrical transport) of 3d transition-metal oxides are delicately sensitive to the occupation of d orbitals.[42] To understand the difference of Mn−Ti exchange coupling at the LSMO/BTO heterointerfaces, we utilize element-specific XAS and XLD (Figure 2B) to probe the electronic structure and orbital occupancy. Figure 4 shows the normalized XAS and XLD signals of Mn- and Ti-L edges measured at 300 K, respectively. The preferential orbital of Mn under the P_{dn} state is in-plane ($d_{x^2-y^2}$ in Figure 4A), verified by a negative XLD integral in Figure S17. The orbital of Mn under P_{up} is out-of-plane ($d_{3z^2-r^2}$ in Figure 4C) confirmed by a positive XLD integral in Figure S17. However, both Ti preferential orbitals under P_{dn} (Figure 4B) and P_{up} (Figure 4D) states are out-of-plane ($d_{xz/yz}$), which is consistent with an elongated c axis under compressive strain from the substrate (tetragonality of BTO is 1.1). The change of orbital occupation tuned by FE field effect is further supported by the orbital-resolved density of states (DOS, Figure 4E,F) based on density functional
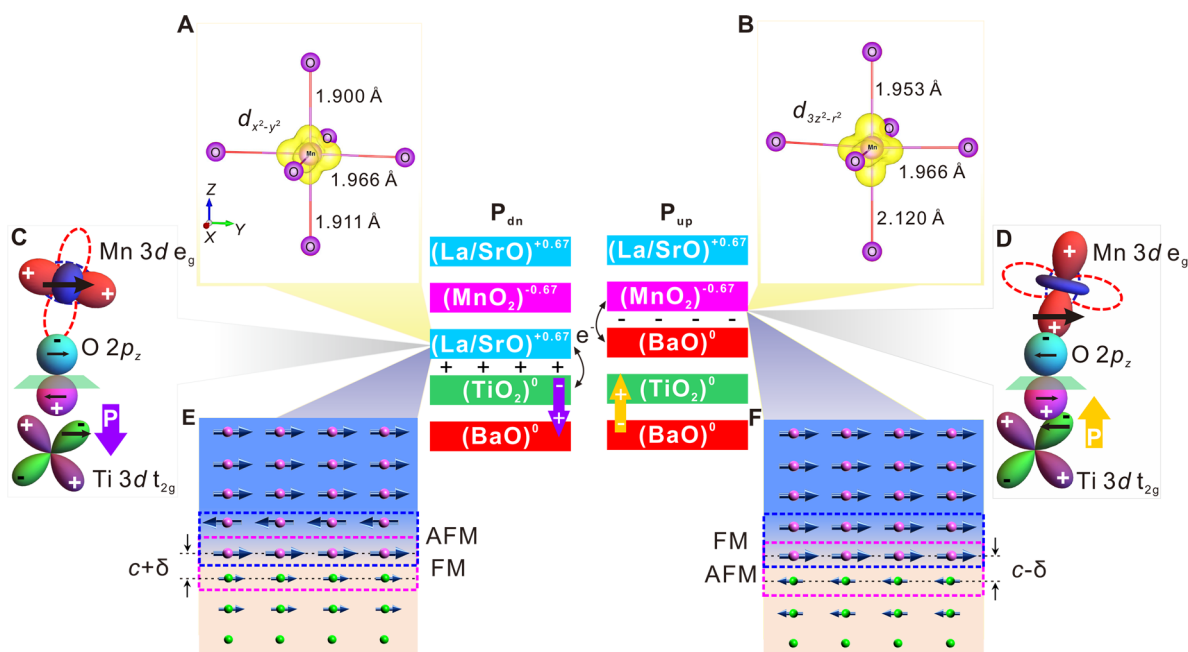
Figure 5. Mn orbital occupation and interfacial magnetic couplings across the Titanite/Manganite interfaces. (A) and (B) Real-space charge density calculated in the energy window from E_F-0.94 eV to E_F (E_F is the Fermi energy) at the LaO/TiO interface (A) and the BaO/MnO interface (B) in the LSMO/BTO heterostructure. The Mn−O bond lengths are indicated. (C) and (D) The sketches of the orbital hybridization between Mn and Ti via O. The black arrows represent the spin alignment based on the Goodenough rules. (E) and (F) Proposed interfacial spin configuration and magnetic coupling mechanism at the LSMO/BTO heterointerfaces. The center shows the charge redistribution at the interfaces. The black ± symbols represent the screening charges induced by the FE bond charges.

theory (DFT) calculations (further details can be found in the Supporting Information). The structural distortion of interfacial MnO_6 octahedra under a tensile strain from the BTO layer (Figure S4C and Table S1) and the alteration of Mn−O bond from FE field is the primary origin of orbital anisotropy. This configuration of orbital degeneration as determined by FE polarization is consistent with the theoretical predictions[43] and experimental observations.[14,44]

Discussion. Combining the microscopic element-specific XMCD and XLD results and the macroscopic magnetic properties with EELS analysis, we now turn to construct a picture of the mutual effects at the FE/FM interface regarding the charge redistribution, orbital anisotropy, and possible interfacial magnetic arrangement between Mn and Ti moments. The charge redistribution originating from the competition of charge transfer/oxygen vacancy and FE screening charge at the interfaces leads to transferred electrons on the Ti d orbitals and thus an induced magnetism on the Ti atom. It is believed that the tensile stress from the substrate and the Jahn−Teller effect lead to a smaller Mn−O bond length (3.81 Å) along the out-of-plane than that along the in-plane,[45] as shown in Figure 5A; thus electron occupation of the Mn $d_{x^2-y^2}$ orbital is energetically preferred. In the FE/FM heterostructure, the FE polarization effect should be considered as well. For the P_{dn} state, the FE field leads to a further reduction in the out-of-plane Mn−O bond length via distortion of the oxygen octahedra,[43] therefore, electrons still preferably occupy the Mn $d_{x^2-y^2}$ orbital. On the contrary, for the P_{up} state, the FE field leads to a substantially elongated Mn−O bond (4.01 Å) along the out-of-plane (Figure 5B) via overcoming the tensile stress from STO substrate; thus the Mn $d_{3z^2-r^2}$ orbital is preferentially occupied. The layer-resolved lattice parameters extracted from the STEM images (Figure S21) suggest that the out-of-plane lattice parameter (3.99 Å) of

the first unit cell of LSMO close to the interface for the P_{up} sample is indeed larger than that (3.80 Å) for the P_{dn} sample. Both the XLD and XMCD signals from the O-K edge (Figures S18 and S19) further confirm that the hybridization of Mn− O−Ti is stronger for the P_{up} state than that for the P_{dn} state. The hybridization between the Mn occupied $d_{x^2-y^2}$ orbital and the Ti $d_{xz/yz}$ orbital across the interface is very weak due to the larger Mn−Ti distance ($c + \delta$) in the heterostructure with the P_{dn} state, where δ is FE displacement of ions; thus the virtual hopping of electron is limited. According to the Goodenough− Kanamori rules,[46] the virtual hopping of electron from the occupied Ti orbital to the empty Mn $d_{3z^2-r^2}$ orbital determines the FM coupling between Mn and Ti, as shown in Figure 5C. Also, for the P_{dn} state, the small magnetic moment of Mn atom and a weak exchange bias (Figure S10) may be possibly due to the presence of an AFM layer at the interface.[33] We therefore propose that in the P_{dn} heterostructure, the exchange coupling between Mn atoms at the interface is AFM, whereas it is FM between Mn and Ti, as shown in Figure 5E. On the contrary, in the P_{up} heterostructure, there is a strong overlap and hybridization across the interface between the occupied Mn $d_{3z^2-r^2}$ orbitals and Ti $d_{xz/yz}$ orbitals due to the reduced distance between Mn and Ti ($c − \delta$), as shown in Figure 5D. According to the Goodenough−Kanamori rules and the interfacial orbital hybridization,[37,47] magnetic moments of Ti t_{2g} electrons and the half-filled Mn bands should be AFM coupled at the interface, as shown in Figure 5F. Interfacial AFM magnetic coupling in LSMO/LSCO[48] or LSMO/BFO,[49] LCMO/ BFO,[50] and LSMO/LFO[18] have been previously reported, where the magnetic moments in Cu or Fe atoms are pre-existing. However, in our samples, charge redistribution changes nonmagnetic Ti^{4+} (d^0) in bulk BTO to magnetic Ti^{3+} (d^1) at heterointerface, and magnetic coupling is tuned by

the FE polarization, which is fundamentally different from the other studies.

Conclusion. In summary, we have explored the FE field effect on the orbital hybridization and induced magnetism at the Titanite-Manganite heterointerfaces and showed that charge redistribution and changes in orbital occupancy play an important role. The element-specific XMCD spectra indicated that FE polarization controls the spin and orbital moments of the interfacial Mn and Ti atoms and affects the interfacial exchange interaction. The combination of atomic-resolution STEM and EDX mapping with EELS characterization provided a detailed picture of charge redistribution and changes in the valence states across oxide heterointerfaces. Both XLD characterization and the calculated orbital-resolved DOS confirmed the polarization-dependent orbital occupancy, activating the FE control of the interfacial exchange coupling. Our findings demonstrate a route to the electrical control of magnetic states and interactions at the oxide FM/FE heterointerfaces, which in turn tunes the spin-dependent transport properties in magnetic and FE tunnel junctions.

Materials and Methods. *Sample Preparation.* All LSMO/BTO heterostructures were epitaxially grown on atomically smooth (001) STO single-crystal substrates (CrysTec GmbH) by pulsed laser deposition (PLD). One u.c.-SRO layer were predeposited on TiO_2-terminated STO substrates, resulting in a SrO-terminated surface. After film growth, pure oxygen (typically 200 Torr annealing for 1 h) was introduced to the PLD chamber, and the samples were cooled down to room temperature at a cooling rate of 10 °C min^{-1} to reduce oxygen vacancy.

Sample Characterization. The surface morphology and ferroelectricity of these as-grown heterostructures were characterized by AFM and PFM on a commercial scanning probe microscope (Asylum Research MFP-3D) instrument at room temperature. The crystal structures and strain state were characterized by synchrotron-based X-ray diffraction at room temperature. Microstructure, interfacial structure, element mappings, and EELS were conducted by aberration-corrected STEM (FEI Titan G2 80-200 microscope equipped with a Super-X EDX detector) at room temperature. The magnetization measurements at different temperatures were conducted by a superconducting quantum interference device (SQUID). XAS signals were recorded from the total electron yield (TEY) current, which takes into account the surface sensitivity (with a 30° grazing angle) and element selectivity of the TEY mode. X-ray absorption spectroscopy (XAS) was conducted at room temperature and 80 K at beamline Surface, Interface, and Nanostructure Science of SSLS. The experimental configurations of X-ray linear dichroism (XLD) and X-ray magnetic circular dichroism (XMCD) are shown in Figure 2B. The XLD signal is obtained by subtracting the intensities of the linear-polarized X-ray with vertical (I_c) polarization from horizontal (I_{ab}) polarization without magnetic field, that is, XLD = $(I_{ab} - I_c)$. The XMCD signal is the difference of the circularized X-ray absorption spectra taken in plus and minus 1 T in-plane magnetic field, that is, XMCD = $(I^+ - I^-)$.

Others. The detailed information on the film growth, characterization, and DFT calculations are listed in Supporting Information.

ASSOCIATED CONTENT

ⓢ Supporting Information

The Supporting Information is available free of charge on the ACS Publications website at DOI: 10.1021/acs.nanolett.9b00441.

Detailed information on the film growth, characterization, determination of cation displacement vector, DFT calculations, and the estimation of spin and orbital moments (PDF)

AUTHOR INFORMATION

Corresponding Authors
*E-mail: msecj@nus.edu.sg.
*E-mail: hetian@zju.edu.cn.

ORCID
Rui Guo: 0000-0002-3733-8908
ZhiLi Dong: 0000-0001-8116-6747
Gan Moog Chow: 0000-0001-7634-4553
Jingsheng Chen: 0000-0003-3188-2803

Author Contributions
○These authors contributed equally to this work. H.W. and J.S.C. conceived and designed this work and wrote the manuscript. H.W. conducted the sample preparation and characterization and data analysis. X.C., J.S.C., C.J.S., and G.M.C. conducted the XAS characterization and data analysis. L.L.T. and E.Y.T. conducted the density functional calculation and data analysis. Z.R.L. and H.T.: HAADF-STEM and EELS experiment. J.X.W and Z.L.D. conducted the HR-TEM experiment. H.Y.Y. and P.Y. conducted the XRD. All authors contributed to the manuscript and the interpretation of the data.

Notes
The authors declare no competing financial interest.

REFERENCES

(1) Eerenstein, W.; Mathur, N. D.; Scott, J. F. *Nature* **2006**, *442*, 759.
(2) Bibes, M.; Barthelemy, A. *Nat. Mater.* **2008**, *7*, 425.
(3) Fusil, S.; Garcia, V.; Barthélémy, A.; Bibes, M. *Annu. Rev. Mater. Res.* **2014**, *44*, 91.
(4) Zheng, H.; Wang, J.; Lofland, S. E.; Ma, Z.; Mohaddes-Ardabili, L.; Zhao, T.; Salamanca-Riba, L.; Shinde, S. R.; Ogale, S. B.; Bai, F.; Viehland, D.; Jia, Y.; Schlom, D. G.; Wuttig, M.; Roytburd, A.; Ramesh, R. *Science* **2004**, *303*, 661.
(5) Pantel, D.; Goetze, S.; Hesse, D.; Alexe, M. *Nat. Mater.* **2012**, *11*, 289.

(6) Yin, Y. W.; Burton, J. D.; Kim, Y. M.; Borisevich, A. Y.; Pennycook, S. J.; Yang, S. M.; Noh, T. W.; Gruverman, A.; Li, X. G.; Tsymbal, E. Y.; Li, Q. *Nat. Mater.* **2013**, *12*, 397.

(7) Valencia, S.; Crassous, A.; Bocher, L.; Garcia, V.; Moya, X.; Cherifi, R. O.; Deranlot, C.; Bouzehouane, K.; Fusil, S.; Zobelli, A.; Gloter, A.; Mathur, N. D.; Gaupp, A.; Abrudan, R.; Radu, F.; Barthelemy, A.; Bibes, M. *Nat. Mater.* **2011**, *10*, 753.

(8) Duan, C. G.; Jaswal, S. S.; Tsymbal, E. Y. *Phys. Rev. Lett.* **2006**, *97*, 047201.

(9) Radaelli, G.; et al. *Nat. Commun.* **2014**, *5*, 3404.

(10) Eerenstein, W.; Wiora, M.; Prieto, J. L.; Scott, J. F.; Mathur, N. D. *Nat. Mater.* **2007**, *6*, 348.

(11) Guo, H.; Wang, Z.; Dong, S.; Ghosh, S.; Saghayezhian, M.; Chen, L.; Weng, Y.; Herklotz, A.; Ward, T. Z.; Jin, R.; Pantelides, S. T.; Zhu, Y.; Zhang, J.; Plummer, E. W. *Proc. Natl. Acad. Sci. U. S. A.* **2017**, *114*, No. E5062.

(12) Bingham, N. S.; Suszka, A. K.; Vaz, C. A.; Kim, H.; Heyderman, L. J. *Phys. Rev. B: Condens. Matter Mater. Phys.* **2017**, *96*, 024419.

(13) Wu, S. M.; Cybart, S. A.; Yu, P.; Rossell, M. D.; Zhang, J. X.; Ramesh, R.; Dynes, R. C. *Nat. Mater.* **2010**, *9*, 756.

(14) Cui, B.; Song, C.; Mao, H.; Wu, H.; Li, F.; Peng, J.; Wang, G.; Zeng, F.; Pan, F. *Adv. Mater.* **2015**, *27*, 6651.

(15) Molegraaf, H. J. A.; Hoffman, J.; Vaz, C. A. F.; Gariglio, S.; van der Marel, D.; Ahn, C. H.; Triscone, J.-M. *Adv. Mater.* **2009**, *21*, 3470.

(16) Herklotz, A.; Guo, E. J.; Wong, A. T.; Meyer, T. L.; Dai, S.; Ward, T. Z.; Lee, H. N.; Fitzsimmons, M. R. *Nano Lett.* **2017**, *17* (3), 1665−1669.

(17) Liu, Y.; Tornos, J.; te Velthuis, S. G. E.; Freeland, J. W.; Zhou, H.; Steadman, P.; Bencok, P.; Leon, C.; Santamaria, J. *APL Mater.* **2016**, *4*, 046105.

(18) Bruno, F. Y.; Grisolia, M. N.; Visani, C.; Valencia, S.; Varela, M.; Abrudan, R.; Tornos, J.; Rivera-Calzada, A.; Unal, A. A.; Pennycook, S. J.; Sefrioui, Z.; Leon, C.; Villegas, J. E.; Santamaria, J.; Barthelemy, A.; Bibes, M. *Nat. Commun.* **2015**, *6*, 6306.

(19) Lu, W.; Li, C.; Zheng, L.; Xiao, J.; Lin, W.; Li, Q.; Wang, X. R.; Huang, Z.; Zeng, S.; Han, K.; Zhou, W.; Zeng, K.; Chen, J.; Ariando; Cao, W.; Venkatesan, T. *Adv. Mater.* **2017**, *29*, 1606165.

(20) Cui, B.; Song, C.; Mao, H.; Yan, Y.; Li, F.; Gao, S.; Peng, J.; Zeng, F.; Pan, F. *Adv. Funct. Mater.* **2016**, *26*, 753.

(21) Kim, Y. M.; Morozovska, A.; Eliseev, E.; Oxley, M. P.; Mishra, R.; Selbach, S. M.; Grande, T.; Pantelides, S. T.; Kalinin, S. V.; Borisevich, A. Y. *Nat. Mater.* **2014**, *13*, 1019.

(22) Yu, P.; Luo, W.; Yi, D.; Zhang, J. X.; Rossell, M. D.; Yang, C. H.; You, L.; Singh-Bhalla, G.; Yang, S. Y.; He, Q.; Ramasse, Q. M.; Erni, R.; Martin, L. W.; Chu, Y. H.; Pantelides, S. T.; Pennycook, S. J.; Ramesh, R. *Proc. Natl. Acad. Sci. U. S. A.* **2012**, *109*, 9710.

(23) Guo, R.; Shen, L.; Wang, H.; Lim, Z.; Lu, W.; Yang, P.; Ariando; Gruverman, A.; Venkatesan, T.; Feng, Y. P.; Chen, J. *Adv. Mater. Interfaces* **2016**, *3*, 1600737.

(24) Jiang, L.; Choi, W. S.; Jeen, H.; Dong, S.; Kim, Y.; Han, M. G.; Zhu, Y.; Kalinin, S. V.; Dagotto, E.; Egami, T.; Lee, H. N. *Nano Lett.* **2013**, *13*, 5837.

(25) Vaz, C. A.; Hoffman, J.; Segal, Y.; Reiner, J. W.; Grober, R. D.; Zhang, Z.; Ahn, C. H.; Walker, F. J. *Phys. Rev. Lett.* **2010**, *104*, 127202.

(26) Wang, H.; Liu, Z. R.; Yoong, H. Y.; Paudel, T. R.; Xiao, J. X.; Guo, R.; Lin, W. N.; Yang, P.; Wang, J.; Chow, G. M.; Venkatesan, T.; Tsymbal, E. Y.; Tian, H.; Chen, J. S. *Nat. Commun.* **2018**, *9*, 3319.

(27) Tenne, D. A.; Bruchhausen, A.; Lanzillotti-Kimura, N. D.; Fainstein, A.; Katiyar, R. S.; Cantarero, A.; Soukiassian, A.; Vaithyanathan, V.; Haeni, J. H.; Tian, W.; Schlom, D. G.; Choi, K. J.; Kim, D. M.; Eom, C. B.; Sun, H. P.; Pan, X. Q.; Li, Y. L.; Chen, L. Q.; Jia, Q. X.; Nakhmanson, S. M.; Rabe, K. M.; Xi, X. X. *Science* **2006**, *313*, 1614−6.

(28) Yu, J.; Wu, Z.; Liu, Z.; Yan, Q.; Wu, J.; Duan, W. *J. Phys.: Condens. Matter* **2008**, *20*, 135203.

(29) Jia, C. L.; Mi, S. B.; Urban, K.; Vrejoiu, I.; Alexe, M.; Hesse, D. *Nat. Mater.* **2008**, *7*, 57−61.

(30) Choi, K. J.; Biegalski, M.; Li, Y. L.; Sharan, A.; Schubert, J.; Uecker, R.; Reiche, P.; Chen, Y. B.; Pan, X. Q.; Gopalan, V.; Chen, L. Q.; Schlom, D. G.; Eom, C. B. *Science* **2004**, *306*, 1005−9.

(31) Chen, C. T.; Idzerda, Y. U.; Lin, H.; Smith, N. V.; Meigs, G.; Chaban, E.; Ho, G. H.; Pellegrin, E.; Sette, F. *Phys. Rev. Lett.* **1995**, *75* (1), 152−155.

(32) Burton, J. D.; Tsymbal, E. Y. *Phys. Rev. Lett.* **2011**, *106*, 157203.

(33) Burton, J. D.; Tsymbal, E. Y. *Phys. Rev. B: Condens. Matter Mater. Phys.* **2009**, *80*, 174406.

(34) Junquera, J.; Ghosez, P. *Nature* **2003**, *422*, 506.

(35) Takahashi, K. S.; Matsubara, Y.; Bahramy, M. S.; Ogawa, N.; Hashizume, D.; Tokura, Y.; Kawasaki, M. *Sci. Rep.* **2017**, *7*, 4631.

(36) Lee, J. S.; Xie, Y. W.; Sato, H. K.; Bell, C.; Hikita, Y.; Hwang, H. Y.; Kao, C. C. *Nat. Mater.* **2013**, *12*, 703.

(37) Garcia-Barriocanal, J.; Cezar, J. C.; Bruno, F. Y.; Thakur, P.; Brookes, N. B.; Utfeld, C.; Rivera-Calzada, A.; Giblin, S. R.; Taylor, J. W.; Duffy, J. A.; Dugdale, S. B.; Nakamura, T.; Kodama, K.; Leon, C.; Okamoto, S.; Santamaria, J. *Nat. Commun.* **2010**, *1*, 82.

(38) Varela, M.; Oxley, M. P.; Luo, W.; Tao, J.; Watanabe, M.; Lupini, A. R.; Pantelides, S. T.; Pennycook, S. J. *Phys. Rev. B: Condens. Matter Mater. Phys.* **2009**, *79*, 085117.

(39) Ohtomo, A.; Muller, D. A.; Grazul, J. L.; Hwang, H. Y. *Nature* **2002**, *419*, 378.

(40) Nakagawa, N.; Hwang, H. Y.; Muller, D. A. *Nat. Mater.* **2006**, *5*, 204.

(41) Hong, X.; Posadas, A.; Ahn, C. H. *Appl. Phys. Lett.* **2005**, *86*, 142501.

(42) Tokura, Y. *Science* **2000**, *288*, 462.

(43) Chen, H.; Qiao, Q.; Marshall, M. S.; Georgescu, A. B.; Gulec, A.; Phillips, P. J.; Klie, R. F.; Walker, F. J.; Ahn, C. H.; Ismail-Beigi, S. *Nano Lett.* **2014**, *14*, 4965.

(44) Preziosi, D.; Alexe, M.; Hesse, D.; Salluzzo, M. *Phys. Rev. Lett.* **2015**, *115*, 157401.

(45) Pesquera, D.; Herranz, G.; Barla, A.; Pellegrin, E.; Bondino, F.; Magnano, E.; Sanchez, F.; Fontcuberta, J. *Nat. Commun.* **2012**, *3*, 1189.

(46) Goodenough, J. B. *Phys. Rev.* **1955**, *100*, 564.

(47) Okamoto, S. *Phys. Rev. B: Condens. Matter Mater. Phys.* **2010**, *82*, 024427.

(48) De Luca, G. M.; Ghiringhelli, G.; Perroni, C. A.; Cataudella, V.; Chiarella, F.; Cantoni, C.; Lupini, A. R.; Brookes, N. B.; Huijben, M.; Koster, G.; Rijnders, G.; Salluzzo, M. *Nat. Commun.* **2014**, *5*, 5626.

(49) Yu, P.; Lee, J. S.; Okamoto, S.; Rossell, M. D.; Huijben, M.; Yang, C. H.; He, Q.; Zhang, J. X.; Yang, S. Y.; Lee, M. J.; Ramasse, Q. M.; Erni, R.; Chu, Y. H.; Arena, D. A.; Kao, C. C.; Martin, L. W.; Ramesh, R. *Phys. Rev. Lett.* **2010**, *105*, 027201.

(50) Yi, D.; Liu, J.; Okamoto, S.; Jagannatha, S.; Chen, Y.-C.; Yu, P.; Chu, Y.-H.; Arenholz, E.; Ramesh, R. *Phys. Rev. Lett.* **2013**, *111*, 127601.